Engineering 3 (2017) 393–401

Contents lists available at ScienceDirect

Engineering

journal homepage: www.elsevier.com/locate/eng

Research
Green Chemical Engineering—Article

Harnessing the Beneficial Attributes of Ceria and Titania in a Mixed-Oxide Support for Nickel-Catalyzed Photothermal CO_2 Methanation

Ee Teng Kho, Salina Jantarang, Zhaoke Zheng, Jason Scott*, Rose Amal*

Particles and Catalysis Research Laboratory, School of Chemical Sciences and Engineering, The University of New South Wales, Sydney, NSW 2052, Australia

ARTICLE INFO

Article history:
Received 24 January 2017
Revised 5 April 2017
Accepted 27 April 2017
Available online 17 May 2017

Keywords:
Photothermal
CO_2 reduction
Nickel
Ceria
Titania

ABSTRACT

Solar-powered carbon dioxide (CO_2)-to-fuel conversion presents itself as an ideal solution for both CO_2 mitigation and the rapidly growing world energy demand. In this work, the heating effect of light irradiation onto a bed of supported nickel (Ni) catalyst was utilized to facilitate CO_2 conversion. Ceria (CeO_2)-titania (TiO_2) oxide supports of different compositions were employed and their effects on photothermal CO_2 conversion examined. Two factors are shown to be crucial for instigating photothermal CO_2 methanation activity: ① Fine nickel deposits are required for both higher active catalyst area and greater light absorption capacity for the initial heating of the catalyst bed; and ② the presence of defect sites on the support are necessary to promote adsorption of CO_2 for its subsequent activation. Titania inclusion within the support plays a crucial role in maintaining the oxygen vacancy defect sites on the (titanium-doped) cerium oxide. The combination of elevated light absorption and stabilized reduced states for CO_2 adsorption subsequently invokes effective photothermal CO_2 methanation when the ceria and titania are blended in the ideal ratio(s).

© 2017 THE AUTHORS. Published by Elsevier LTD on behalf of the Chinese Academy of Engineering and Higher Education Press Limited Company. This is an open access article under the CC BY-NC-ND license (http://creativecommons.org/licenses/by-nc-nd/4.0/).

1. Introduction

The recycling of carbon dioxide (CO_2) into fuel is an attractive solution to mitigate CO_2 emissions and address the growing global energy demand. However, the relative thermodynamic stability of CO_2 poses a great challenge for its effective conversion without high energy consumption. Such energy consumption is often provided in the form of fossil fuel-derived heat. The need for a green and sustainable energy source is the primary motivation behind the potential utilization of sunlight for heat provision to achieve renewable catalytic recycling of CO_2.

Solar heating primarily relies on increased atomic vibrational energy due to solar radiation absorption. Through such a route, high temperatures are achievable via the concentration of sunlight. Localized surface plasmon resonance (LSPR) also occurs to facilitate photothermal catalysis, which has been gaining increased attention for catalytic applications [1–5]. The resonance of oscillating free electrons on the surface of a conducting material upon interaction with impending electromagnetic wave(s) of specific wavelength(s) can result in the dissipation of intense heat energy within the vicinity of the plasmonic particle. If a plasmonic material (e.g., metal) is coupled with catalytic capabilities, the localized hotspots can also assist with the activation of a reactant molecule. The work of Wang et al. [6], which involved a zinc oxide-supported gold catalyst, shows that this application is possible for CO_2 reduction. Although they do not explicitly discuss the photothermal heating aspects, Meng et al. [7] also successfully demonstrated a similar light-for-heat concept for CO_2 hydrogenation, in which a catalyst bed temperature of approximately 400 °C was achieved and measured under light illumination. Another interesting finding of the work was that a reducible oxide (titania)-supported metal demonstrated enhanced CO_2 conversion as compared with the insulator (aluminum oxide)-supported equivalent.

The use of reducible oxides coupled with metal catalysts to achieve activity enhancement is not unusual. In addition to the benchmark copper/zinc oxide catalyst, reducible oxides such as titania

* Corresponding author.
E-mail addresses: jason.scott@unsw.edu.au; r.amal@unsw.edu.au

http://dx.doi.org/10.1016/J.ENG.2017.03.016
2095-8099/© 2017 THE AUTHORS. Published by Elsevier LTD on behalf of the Chinese Academy of Engineering and Higher Education Press Limited Company. This is an open access article under the CC BY-NC-ND license (http://creativecommons.org/licenses/by-nc-nd/4.0/).

(TiO_2) and ceria (CeO_2) have been commonly studied for CO_2 catalysis [8–10], which is attributed to the formation of an active metal oxide interface upon the utilization of such oxides. For CO_2 reduction reactions, Graciani et al. [11] and Yang et al. [12] demonstrated the role of an active interface in improving CO_2-to-methanol conversion for ceria-titania binary oxides coupled with copper and gold metals, respectively. The combination of cerium and titanium oxides has been shown to lead to the stabilization of reduced ceria (CeO_x, $x < 2$) species [13–15]. These reduced species have been reported to aid in the dispersion of deposited surface metal [16,17] and surface charge redistribution within metal nanoparticles near the metal oxide interface [12], which subsequently facilitate CO_2 adsorption and activation.

In our preceding study [18], the unique redox capabilities of cerium-titanium oxide particles were utilized for the (low-temperature) steam reforming of methane. The progression in material properties across varied compositions (and synthesis pathways) was studied to examine the effect on catalytic reforming. Here, as an extension to our prior investigation, we examine ceria-titania-supported nickel (Ni) catalyst particles for CO_2 methanation. In contrast to the steam-reforming work [18], and to most CO_2 conversion studies in which energy is supplied in the form of heat, methanation was carried out in a photothermal reaction system in which full-spectrum irradiation was utilized to drive CO_2 reduction reaction. In the earlier work, the ceria-titania-supported nickel particles were characterized according to properties that were important for defining thermal activity and catalyst selectivity (i.e., specific surface area, catalyst morphology, support crystallinity, nickel deposit size, support, and nickel reducibility). Because the current study utilizes light within the system, we assessed the optical properties of the materials via ultraviolet-visible-near-infrared (UV-Vis-NIR) spectroscopy. In addition, as the reaction being examined in this study is CO_2 methanation (as opposed to steam reforming in the prior study), we used analytical techniques that were more relevant to the process (e.g., CO_2 and hydrogen gas (H_2) temperature-programmed desorption (TPD)) and that provided greater insight into the origins of the catalyst performance (i.e., X-ray photoelectron spectroscopy (XPS) and nickel deposit size).

2. Experimental methods

2.1. Catalyst preparation

2.1.1. Ceria-titania mixed-oxide synthesis

The ceria-titania mixed oxides (*x*Ce-*y*Ti) were prepared via a sol-gel route as previously described in Ref. [18]. In brief, the cerium precursor solution was prepared by dissolving the required amount of hydrated cerium nitrated salt (Aldrich) in 20 mL of ethanol, which was then acidified with 0.36 mL of concentrated nitric acid (Ajax). This solution was added dropwise to a solution containing 10 mL of titanium butoxide (Sigma-Aldrich) diluted with 60 mL of ethanol under continuous magnetic stirring at 300 $r \cdot min^{-1}$. After aging the solution for 48 h, calcination was carried out in a muffle furnace at 550 °C for 3 h, with the ramp rate set to 1 $°C \cdot min^{-1}$. The product was ground into a fine powder. These neat supports are denoted as *x*Ce-*y*Ti_SG, where *x* and *y* indicate the relative mole ratios of cerium and titanium, respectively, and SG signifies the sol-gel synthesis method. Mixed oxides with nominal *x*:*y* ratios of 20:80, 50:50, and 80:20 were studied for this work. Pure titania (TiO_2_SG) and ceria (CeO_2_SG) were also prepared according to the procedure described above.

2.1.2. Impregnation of nickel onto the x*Ce*-y*Ti supports

To produce a catalyst with a nominal nickel loading of 10 wt%, hydrated nickel nitrate salt (Univar) was dissolved into 5 mL of ultrapure water (Millipore, Milli-Q 18.2 MΩ·cm) within which 1 g of the neat *x*Ce-*y*Ti_SG support was suspended. Continuous magnetic stirring was applied over a hot plate to evaporate excess moisture. The resulting slurry was oven-dried at 110 °C overnight. The dried particles were calcined at 400 °C (5 $°C \cdot min^{-1}$ ramp rate, held for 3 h) under a 60 $mL \cdot min^{-1}$ air flow.

To activate the catalyst, the calcined NiO/*x*Ce-*y*Ti_SG samples were reduced under 50 $mL \cdot min^{-1}$ 10 vol% H_2/argon (H_2/Ar) flow at 400 °C (5 $°C \cdot min^{-1}$ ramp rate, held for 1 h) such that Ni/*x*Ce-*y*Ti_SG was obtained.

2.2. Catalyst characterization

UV-Vis-NIR absorption spectra were acquired using a UV-Vis-NIR spectrophotometer (Shimadzu, UV-3600). Transmission electron microscopy (TEM) images were acquired using a TEM microscope (Philips, CM200 FEG) operated at 200 kV. The samples were ultrasonically dispersed in methanol and dripped onto a carbon-coated copper grid for imaging. TPD experiments were performed using a chemisorption analyzer (Micromeritics, AutoChem 2910). For these experiments, the samples (50 mg) were first reduced *in situ* in 10 vol% H_2/Ar flow (50 $mL \cdot min^{-1}$) at 400 °C for 1 h (5 $°C \cdot min^{-1}$) before being cooled to room temperature (under 10 vol% H_2/Ar flow). For H_2-TPD analyses, the samples were next exposed to the same flow of 10 vol% H_2/Ar for 1 h, and then purged with Ar flow (20 $mL \cdot min^{-1}$) for 30 min before the temperature was raised at a rate of 10 $°C \cdot min^{-1}$ to 700 °C under continuous Ar flow. For CO_2-TPD analyses, after reduction and cooling, the samples were first purged with helium (He) flow (20 $mL \cdot min^{-1}$) for 30 min, then exposed to CO_2 flow (20 $mL \cdot min^{-1}$) for 1 h, and finally purged again with He flow for 30 min. The profiles were recorded over a temperature ramp rate of 10 $°C \cdot min^{-1}$ to 700 °C under continuous He flow. Surface elemental analysis and oxidation state evaluation were performed on the reduced catalysts using an X-ray photoelectron spectrometer (Thermo Scientific, ESCALAB 250Xi) with a mono-chromated Al-Kα X-ray source. The X-ray source was operated at 13 kV and 12 mA.

2.3. Catalyst activity assessment

The photothermal reaction was carried out in a (glass) batch reactor with 540 cm^3 volume (illustrated in Fig. 1). The reduced catalysts (0.1 g) were transferred onto a piece of glass fiber prefilter (Merck Millipore Ltd.) and spread over a circular area with a 3 cm diameter. Prior to the reaction, the reactor system was evacuated before being filled with approximately 15 kPa and 60 kPa of CO_2 and H_2, respectively (equivalent to 3 mmol of CO_2 and 12 mmol of H_2). The gas contents were constantly circulated within the reactor using a gas circulating pump. The catalyst film was irradiated from above through a quartz window using a 300 W xenon lamp (Oriel). The contents of the reaction system were periodically sampled and measured with a gas chromatograph (Shimadzu, GC-2010 Plus) equipped with a capillary column (Sigma-Aldrich, Carboxen-1010 PLOT) and a flame ionization detector.

3. Results and discussion

3.1. Material characteristics

3.1.1. Textural properties and crystallography

The textural properties and crystallography of the catalysts are discussed in detail in Ref. [18]. In addition to the previously measured specific surface areas of TiO_2_SG (< 3 $m^2 \cdot g^{-1}$), 20Ce-80Ti_SG (58 $m^2 \cdot g^{-1}$), 50Ce-50Ti_SG (35 $m^2 \cdot g^{-1}$), and CeO_2_SG (74 $m^2 \cdot g^{-1}$), the specific surface area of 80Ce-20Ti_SG was measured to be 49 $m^2 \cdot g^{-1}$. The crystallography of the 80Ce-20Ti_SG sample was found to be similar to that of 50Ce-50Ti_SG, in which a homogeneous cubic

ceria lattice hosts the titanium ions (Fig. S1 in Supplementary Information). No detectable incorporation of nickel into the ceria-titania support was identified. This result was expected, because the heat treatment temperatures (calcination and reduction) applied after the impregnation of nickel (at 400 °C) are insufficient to induce the formation of titanate-like phases.

3.1.2. UV-Vis-NIR absorption

UV-Vis-NIR absorption was measured for the neat supports and reduced catalysts, as shown in Fig. 2. The absorptions of both of the single-phase oxides (TiO_2_SG in Fig. 2(a) and CeO_2_SG in Fig. 2(e)) mainly resided in the ultraviolet region. This result is also reflected by their bandgap energy values of 3.0 eV and 3.2 eV, respectively,

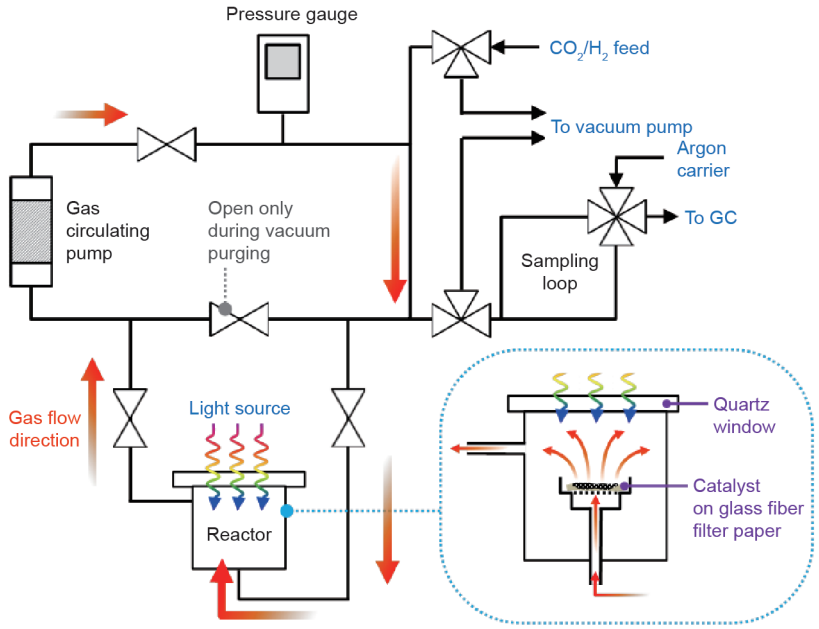

Fig. 1. Configuration of the batch-type photothermal reactor for CO_2 methanation. The inset shows the structure within the reactor. GC: gas chromatograph.

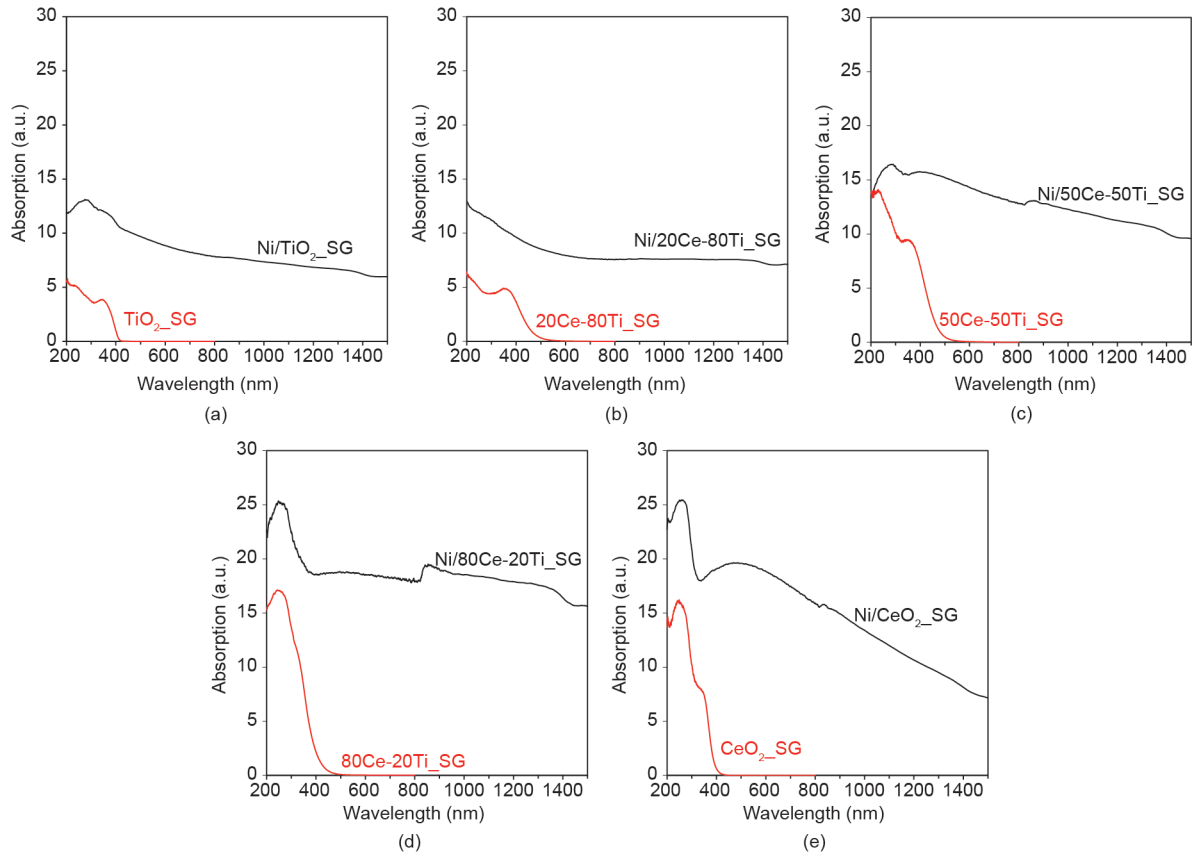

Fig. 2. UV-Vis-NIR absorption spectra (no offset) of nickel catalysts supported on sol-gel-synthesized ceria-titania mixed oxides (black curves): (a) Ni/TiO_2_SG, (b) Ni/20Ce-80Ti_SG, (c) Ni/50Ce-50Ti_SG, (d) Ni/80Ce-20Ti_SG, and (e) Ni/CeO_2_SG. The spectra for the corresponding neat supports are shown in red.

which agree with literature-reported values [19,20]. With the exception of the 80Ce-20Ti_SG neat support, which demonstrated limited visible light absorption (bandgap energy 3.0 eV), significant red shifts were observed for the oxides in which both cerium and titanium were present. The absorption range was extended to about 500 nm for both 20Ce-80Ti_SG (Fig. 2(b)) and 50Ce-50Ti_SG (Fig. 2(c)). The corresponding bandgap energies for both these mixed oxides were calculated to be 2.6 eV. All neat supports demonstrated negligible absorption for wavelengths exceeding 600 nm.

In the presence of reduced nickel species, the absorption intensity is observed to increase across the UV-Vis-NIR light spectrum for all catalysts, as compared with their neat counterparts (the profiles for the nickel-loaded samples have not been offset). This finding is especially noticeable in the NIR region, and is visually verified in that the reduced, nickel-loaded catalysts have a black-colored appearance in comparison with the white or pale yellow colors of the neat supports. No distinct plasmon absorption peak (which is often observed for gold or silver nanoparticles) is observed for the reduced nickel nanoparticles, aside from the increased Vis-NIR absorption. This result is consistent with other literature reports and is usually attributed to the broader absorption characteristics of metallic nickel [21]. Nevertheless, the broad Vis-NIR absorption that was demonstrated for the nickel-loaded samples is favorable for heat generation to drive catalytic conversion.

3.1.3. Nickel deposit size distribution

Nickel deposit size distributions on the different supports were obtained from 200 counts of nickel deposits for each sample (Fig. 3), measured from TEM micrographs. Ni/TiO_2_SG (Fig. 3(a)) and Ni/20Ce-80Ti_SG (Fig. 3(b)) show broad distributions with metal clusters ranging in size from a few nanometers to greater than 60 nm. The dispersion of nickel species is visibly improved for supports with richer cerium content. While the Ni/50Ce-50Ti_SG and Ni/CeO_2_SG catalysts exhibited finer nickel deposit sizes, with the average sizes measured as 11 nm and 13 nm, respectively, Ni/80Ce-20Ti_SG had the narrowest nickel distribution (< 20 nm) and smallest nickel deposit size, averaging at 6 nm. These results indicate that supports with richer cerium content are beneficial for the dispersion of nickel deposits. This finding is consistent with many literature reports in which the presence of cerium within a support is shown to facilitate higher metal dispersion [22–28].

The measured distribution of nickel deposits is also in agreement with the trend demonstrated in the UV-Vis-NIR absorption spectra. Based on the nickel deposit size results, it is expected that the light absorption by nickel on the latter three supports would be stronger than that of the nickel supported by TiO_2_SG and 20Ce-80Ti_SG. This is because larger metal particle sizes are known to decrease light absorption efficiency due to greater scattering effects [29]. As expected, the UV-Vis-NIR absorption spectra of the respective catalysts (Fig. 2) showed that Ni/50Ce-50Ti_SG, Ni/80Ce-20Ti_SG, and Ni/CeO_2_SG had greater light absorption capacities across all three regions (UV, visible, and NIR).

3.1.4. H_2-TPD

Fig. 4 shows the hydrogen desorption behaviors of the (reduced) nickel-loaded oxides. Ni/TiO_2_SG demonstrates negligible hydrogen adsorption at room temperature, which is evident from its lack of distinct desorption peaks. Ni/20Ce-80Ti_SG exhibits both a low-temperature (< 350 °C) and high-temperature (350–600 °C) desorption region, whereas the desorption peaks for Ni/50Ce-50Ti_SG, Ni/80Ce-20Ti_SG, and Ni/CeO_2_SG primarily reside in the low-temperature (< 350 °C) region. The relative areas under the curves also reveal the greater hydrogen adsorption capacity of the ceria-rich catalysts, which is inferred from their dominant low-temperature desorption. From the literature, it is understood that the low-temperature domain of a H_2-TPD curve corresponds to the desorption from the metal surfaces and indicates the fraction of exposed nickel atoms [30–32]. Based on this interpretation, the

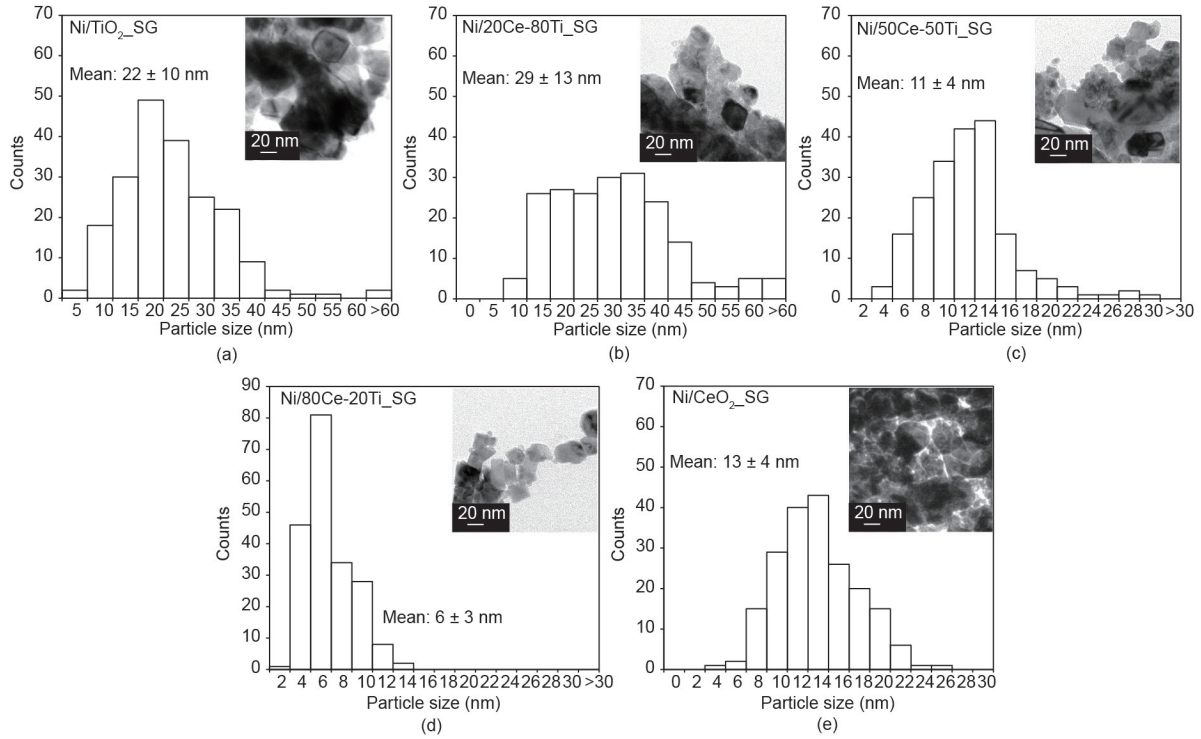

Fig. 3. Nickel deposit size distributions on sol-gel-synthesized ceria-titania mixed-oxide supports with different compositions: (a) Ni/TiO_2_SG, (b) Ni/20Ce-80Ti_SG, (c) Ni/50Ce-50Ti_SG, (d) Ni/80Ce-20Ti_SG, and (e) Ni/CeO_2_SG. The corresponding TEM images are shown as inserts. Each size distribution was obtained from 200 nickel deposit counts.

TPD profiles in Fig. 4 reflect the degree of nickel dispersion, which falls into the following order: Ni/TiO_2_SG < Ni/20Ce-80Ce_SG < Ni/50Ce-50Ti_SG ~ Ni/CeO_2_SG < Ni/80Ce-20Ti_SG. The semi-quantitative nickel dispersion results from the H_2-TPD agree with the results for the nickel deposit size distribution shown earlier in Fig. 3.

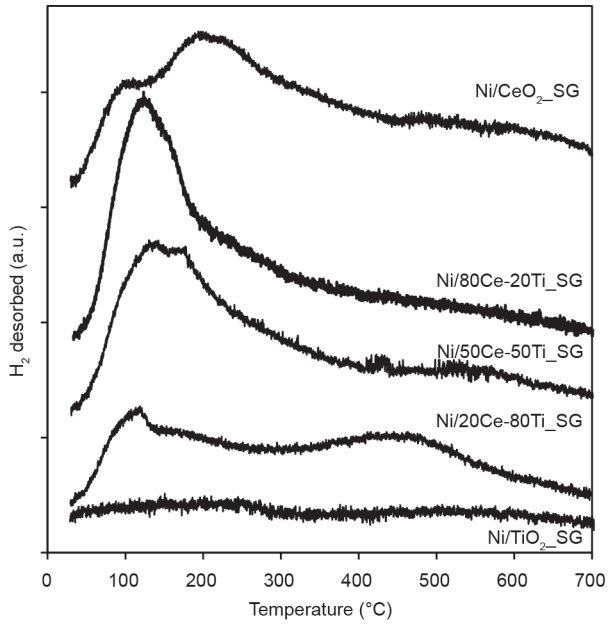

Fig. 4. Amount of H_2 desorbed versus temperature for nickel catalysts supported on sol-gel-synthesized ceria-titania mixed-oxide supports of different compositions. H_2 adsorption was conducted at room temperature for all samples.

3.1.5. CO_2-TPD

The CO_2-TPD technique was used to evaluate the extent of CO_2 binding to the metal/metal oxide samples. In Fig. 5, it is apparent that the cerium-containing metal oxide supports are capable of significant CO_2 adsorption even without the presence of metallic nickel. Negligible (room-temperature) CO_2 adsorption is observed for both TiO_2_SG and Ni/TiO_2_SG.

As a weak Lewis acid, CO_2 can adsorb onto the basic sites of a metal oxide [33]. Fig. 5 shows that the adsorption capacities of the neat metal oxides increase with increasing cerium content, indicating that the presence of cerium increases the surface Lewis basicity of the metal oxides. Since Lewis basicity is defined as the ability of a substance to donate electron pairs, the abovementioned observation implies that the presence of cerium increases the availability of electrons for improved CO_2 adsorption upon the Ce-Ti oxides. One of the known properties of cerium oxide is its reducibility and defect-rich chemistry under a reducing atmosphere. Therefore, the reduction pretreatment that was intended to reduce the nickel oxide in order to active the metallic nickel simultaneously resulted in the reduction of the surface cerium oxide species. As a result, the pretreatment created electron-rich defect sites that encouraged the binding of CO_2 onto these sites. Therefore, the result in Fig. 5 implies that a cerium presence is important to facilitate defect formation and thereby facilitate CO_2 adsorption. Considering that the majority of the adsorbed CO_2 is desorbed at relatively low temperatures (≤ 120 °C), these adsorbed species are not considered to be strongly bound to the catalyst surface when adsorbed at room

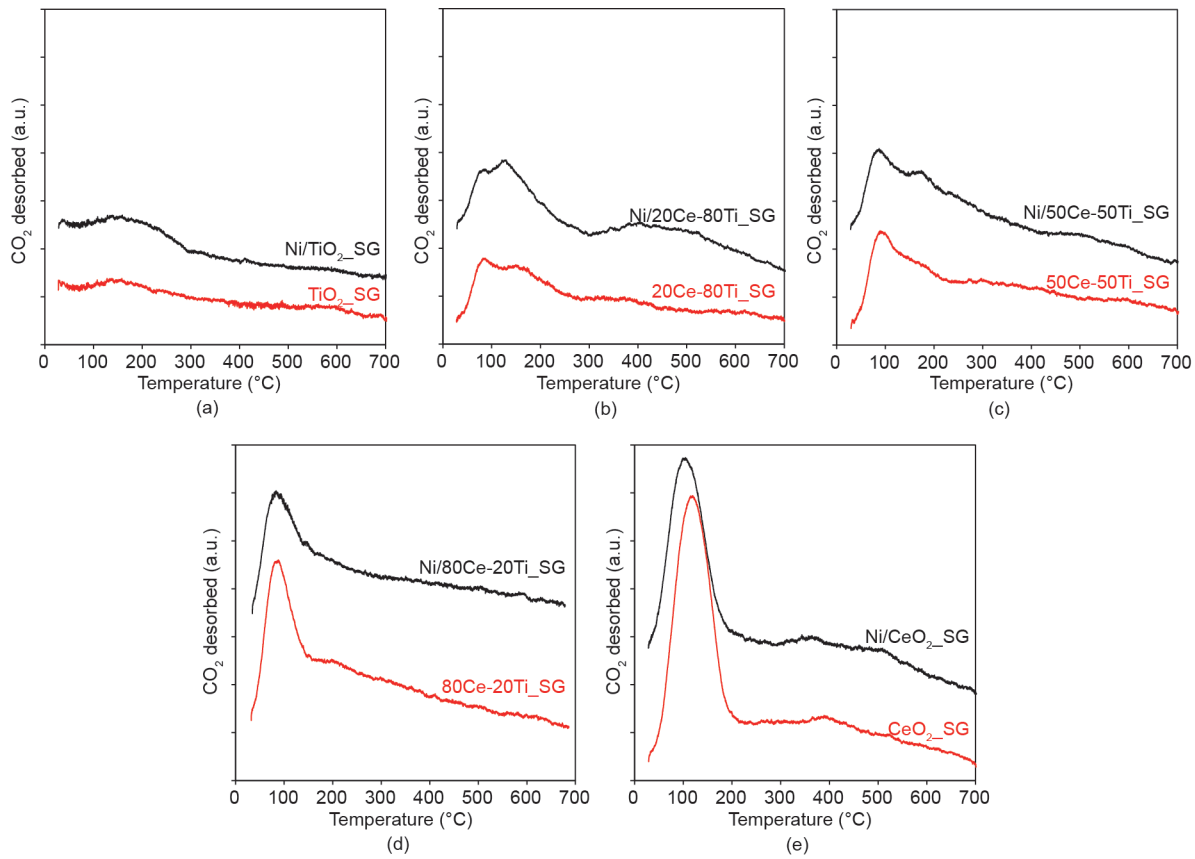

Fig. 5. Amount of CO_2 desorbed with respect to temperature for nickel catalysts supported on sol-gel-synthesized ceria-titania mixed-oxide supports (black curves) with different compositions: (a) Ni/TiO_2_SG, (b) Ni/20Ce-80Ti_SG, (c) Ni/50Ce-50Ti_SG, (d) Ni/80Ce-20Ti_SG, and (e) Ni/CeO_2_SG. The profiles of the respective neat supports are shown in red. CO_2 adsorption was conducted at room temperature for all samples.

temperature.

Regarding the lack of enhanced CO_2 adsorption in the presence of the reduced metallic nickel phase, it has been established that CO_2 has negligible adsorption on Ni(111) sites at room temperature due to its endothermic nature [34–36]. Due to the relative thermodynamic stability of the {111} family, Ni(111) is usually present as the dominant facet of metallic nickel when metallic nickel is synthesized via the impregnation method. This was found to be the case for the catalysts used in this work, as confirmed via X-ray diffraction (XRD) (Ref. [18] and Fig. S1 in Supplementary Information). This comparison thus reveals that the ceria-rich supports primarily provide adsorption sites for CO_2 activation.

3.1.6. XPS elemental analysis

The survey scans (Fig. S2 in Supplementary Information) show the elements detected on the surface of all five (pre-reduced) catalysts. Peaks corresponding to nickel (Ni2p), oxygen (O1s), and titanium (Ti2p) were found for Ni/TiO_2_SG, and peaks corresponding to nickel (Ni2p), oxygen (O1s), and cerium (Ce3d) were found for Ni/CeO_2_SG. Signals belonging to carbon (C1s) were present in all samples and originate from atmospheric carbon contamination.

Although it was anticipated that both cerium- and titanium-related peaks would be observable for the mixed-oxide-supported catalysts, the cerium signals for Ni/20Ce-80Ti_SG were weak (Table 1), indicating its limited presence at the catalyst surface. For both Ni/20Ce-80Ti_SG and Ni/50Ce-50Ti_SG, the amount of surface cerium species was measured to be lower than their respective nominal values. Both this observation and the fact that Ni/20Ce-80Ti_SG has the lowest nominal concentration of cerium justify the lack of defined signal resolution for cerium on its surface.

Fig. 6 presents the $Ni2p_{3/2}$ spectra, in which each Ni2p spectrum is deconvoluted into four peaks, indicating re-oxidation of the nickel surface into different oxidation states for all samples. In addition to a satellite peak at about 861 eV, the binding energies for Ni^0, Ni^{2+}, and Ni^{3+} are assigned at 852.6 eV, 854.6 eV, and 856.1 eV, respectively, for the $Ni2p_{3/2}$ spectra [37]. Taking into account the relative strengths

Table 1
Surface percentage of Ce species and atomic distribution of Ni^0, Ni^{2+}, and Ni^{3+} species based on their corresponding peaks at 852.6 eV, 854.6 eV, and 856.1 eV, respectively.

Catalyst	Surface Ce species[a] (%)	Distribution of surface Ni species		
		Ni^0 (%)	Ni^{2+} (%)	Ni^{3+} (%)
Ni/TiO_2_SG	—	18	44	38
Ni/20Ce-80Ti_SG	2.8 (4)	25	46	29
Ni/50Ce-50Ti_SG	6.2 (10)	23	46	31
Ni/80Ce-20Ti_SG	17.9 (16)	12	55	33
Ni/CeO_2_SG	20.0	9	54	37

[a] Overall surface concentration. The expected surface concentration based on nominal Ce : Ti ratios (using the surface concentration found for Ni/CeO_2_SG as the reference) are given in the brackets.

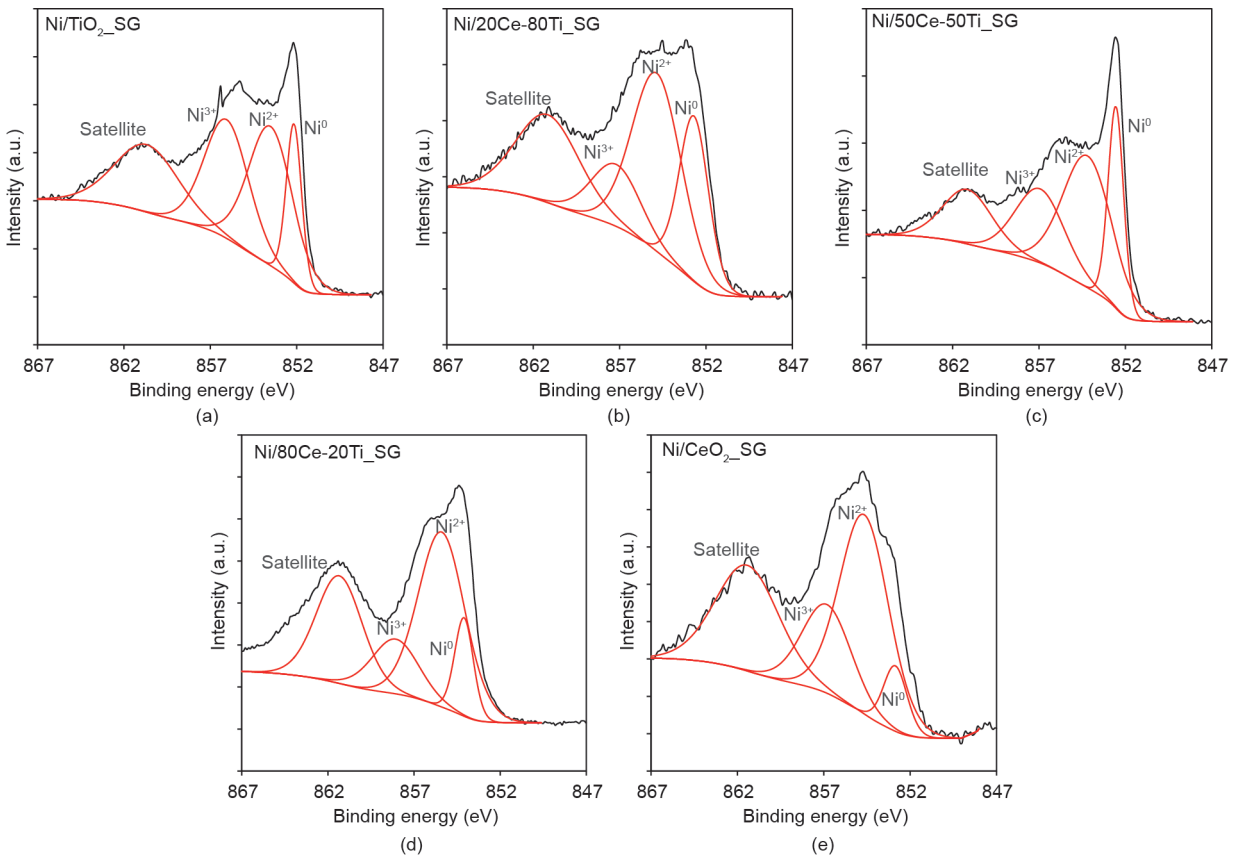

Fig. 6. XPS Ni2p spectra (black curves) of: (a) Ni/TiO_2_SG, (b) Ni/20Ce-80Ti_SG, (c) Ni/50Ce-50Ti_SG, (d) Ni/80Ce-20Ti_SG, and (e) Ni/CeO_2_SG. The deconvolution of each spectrum is shown by the red curves.

of the metallic nickel signals in their respective XPS spectra, and the fact that element detection for XPS analysis only penetrates to a depth of a few nanometers at the surface, the bulk of the nickel clusters should remain in their reduced metallic state beneath the oxidized surface. Such passivation most likely occurred due to oxygen exposure during sample transfer (since oxygen is present in the atmosphere).

Comparing the Ce3d spectra of Ni/50Ce-50Ti_SG and Ni/80Ce-20Ti_SG with that of Ni/CeO_2_SG (Fig. 7) reveals that a titanium presence within the cubic ceria lattice facilitates the preservation of the defective ceria surface after reduction treatment. A Ce3d spectrum is interpreted as follows: the u and v peaks correspond to the $3d_{3/2}$ and $3d_{5/2}$ states, respectively; the u/v and u″/v″ doublets are shakedown features arising from the transfer of electron(s) from a filled O2p orbital to an empty Ce4f orbital [38,39]; photoemissions from Ce^{4+} states are indicated by the u‴/v‴ doublets, and the u′/v′ doublets denote the Ce^{3+} (i.e., reduced cerium oxide) states; in addition to the u′/v′ doublets, the presence of u_0/v_0 doublets signifies the presence of oxygen vacancies [38,40]. The Ce3d spectra in Fig. 7 show that Ce^{4+} is present in all cerium-rich samples (Ni/50Ce-50Ti_SG, Ni/80Ce-20Ti_SG, and Ni/CeO_2_SG). Although reduced Ce^{3+} peaks (u′/v′ doublets) are detected for all three samples, the presence of oxygen vacancy sites is only detected for the Ni/50Ce-50Ti_SG and Ni/80Ce-20Ti_SG samples. This observation implies that the addition of titanium into the cubic lattice of ceria provides a surface that is richer in oxygen vacancy sites and thus possesses a greater electron density.

However, there is a discrepancy between this observation and the earlier CO_2-TPD findings that implied that CeO_2_SG had a greater surface electron density in comparison with both 50Ce-50Ti_SG and 80Ce-20Ti_SG. This apparent conflict in the findings can be accounted for by revisiting the experimental procedure. During the CO_2-TPD experiment, the catalyst was reduced *in situ* and was kept under an inert helium flow. Although the catalysts were also pre-reduced for the XPS analysis, the handling of the samples between catalyst preparation and analysis involved exposure (albeit limited) to non-inert conditions, thus causing the catalyst to come into contact with atmospheric oxygen. This occurrence was demonstrated earlier in the Ni2p spectra, which showed that passivation of the catalyst surface took place during sample transfer after the reduction treatment. Once this factor is taken into account, it is reasoned that although CeO_2_SG shows a higher degree of reduction after hydrogen treatment, upon exposure to air, it is more inclined to the rapid re-oxidation of its surface as compared with 50Ce-50Ti_SG. The results demonstrate the importance of having a titanium presence within a ceria lattice to preserve the stability of the oxygen vacancy sites.

The influence of a titanium presence on the surface characteristics of cerium oxide has been observed by Rodriguez and coworkers [13–15] in their work on CeO_x/TiO_2 composites. Their results, both theoretical and experimental, revealed that the presence of TiO_2 leads to better stability (and thus to a greater tendency for the formation) of Ce^{3+} species. As the observations in the current study demonstrated that the catalyst support has a preference for oxygen vacancy-type species rather than for Ce^{3+}, this comparison also highlights the influence of a mixed-oxide configuration on the electronic characteristics within the material. Whereas the active ceria-titania oxides utilized in this work comprise a ceria lattice doped with titanium ions, the materials studied in Refs. [13–15] consisted of CeO_x nanoparticles deposited upon TiO_2 substrates (i.e., segregated Ti and Ce oxide phases). Nevertheless, both results demonstrate the advantageous outcome of strategically combining ceria with titanium (oxides) for CO_2 conversion purposes.

3.2. Photothermal CO_2 methanation activity

Fig. 8 presents the activities of the catalysts in terms of methane production. Of the five tested catalysts, Ni/50Ce-50Ti_SG and Ni/80Ce-20Ti_SG demonstrated a significantly greater methane production performance than the other catalysts, with the latter exhibiting the fastest conversion rate. Whereas Ni/50Ce-50Ti_SG and Ni/80Ce-20Ti_SG attained complete CO_2 conversion within 180 min and 90 min, respectively, the other catalysts demonstrated minimal conversion within the 180-min duration. Methane-generation rates were calculated (Table 2) and the values obtained for both active catalysts were found to be two orders of magnitude greater than those for the other catalysts. The lack of methane generation for the other three samples was confirmed to be strictly due to ineffective CO_2 conversion, as no other products were detected for any of the catalysts tested.

Although purely photocatalytic CO_2 reduction with H_2 has been shown to be possible over light-active semiconductors, the conversion rates are often limited to micromole efficiencies despite long reaction periods [2,41–44]. Therefore, to achieve the conversion rates demonstrated by Ni/50Ce-50Ti_SG and Ni/80Ce-20Ti_SG, thermal energy must be involved. It is understood from the literature that temperatures greater than 200 °C are often required to drive effective methanation activity [45]. As discussed previously, smaller nickel deposit sizes lead to increased light absorption, and absorption of the NIR spectrum can commence the initial photothermal heating of the catalyst bed. Whereas the poor performance

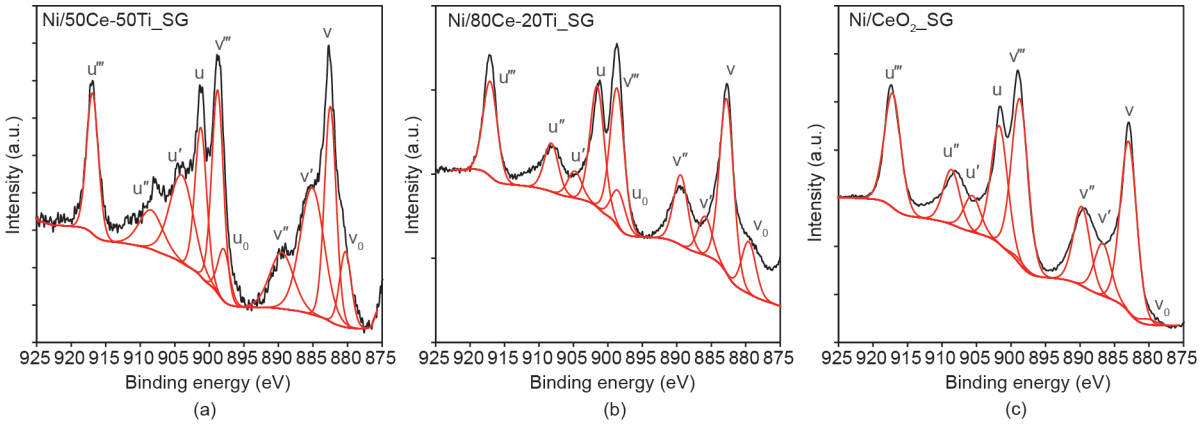

Fig. 7. Ce3d spectra (black curves) of (a) Ni/50Ce-50Ti_SG, (b) Ni/80Ce-20Ti_SG, and (c) Ni/CeO_2_SG. The deconvolution of each spectrum is shown by the red curves. The Ce3d spectrum of Ni/20Ce-80Ti_SG is not shown due to the low surface Ce content, which led to poor peak resolution. The u′/v′ doublets denote Ce^{3+} states, the u‴/v‴ doublets denote Ce^{4+} states, and the u_0/v_0 doublets signify the presence of oxygen vacancies.

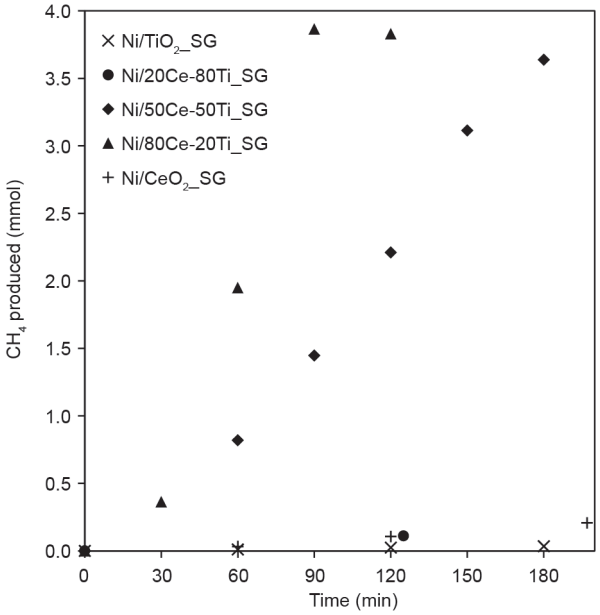

Fig. 8. Amount of CH_4 produced over time by nickel catalysts supported on sol-gel-synthesized ceria-titania mixed-oxide supports with different compositions. Approximately 15 kPa of CO_2 (about 3 mmol) and 60 kPa of H_2 (about 12 mmol) were initially fed into the reactor system, and the catalyst bed (containing 0.1 g reduced catalyst) was illuminated with a 300 W xenon lamp.

Table 2
Methane production rates by supported nickel catalysts.

Catalyst	CH_4 production rate (mmol·(g_{cat}·h)$^{-1}$)
Ni/TiO_2_SG	0.1
Ni/20Ce-80Ti_SG	0.5
Ni/50Ce-50Ti_SG	10.6
Ni/80Ce-20Ti_SG	17.0
Ni/CeO_2_SG	0.7

Approximately 15 kPa of CO_2 (about 3 mmol) and 60 kPa of H_2 (about 12 mmol) were initially fed into the reactor system, and the catalyst bed (containing 0.1 g reduced catalyst) was illuminated with a 300 W xenon lamp.

of Ni/TiO_2_SG and Ni/20Ce-80Ti_SG probably stemmed from their large nickel deposit sizes, a comparison of the UV-Vis-NIR absorption spectra, deposit size distributions, and TPD results suggests that Ni/CeO_2_SG should have similar CO_2 methanation activity to that of Ni/50Ce-50Ti_SG, based on the abovementioned argument. Furthermore, the CO_2-TPD results showed the CeO_2_SG-supported catalyst to have the highest CO_2 adsorption capacity out of the catalysts tested. However, as observed in the XPS results, the defective surface of Ni/CeO_2_SG is prone to rapid re-oxidation upon exposure to atmospheric conditions. Due to the need to transfer activated catalysts between the reduction rig and the methanation reactor, even though the CO_2-TPD indicated that Ni/CeO_2_SG possessed the highest CO_2 adsorption capability, the instability of the CO_2 adsorption sites (i.e., oxygen vacancy sites) upon exposure to atmospheric oxygen ultimately led to the loss of this advantage. As a result, despite the effective light absorption by the small nickel particles for catalyst bed heating, the lack of active sites for CO_2 adsorption led to a subsequent poor performance by Ni/CeO_2_SG. In contrast, Ni/50Ce-50Ti_SG and Ni/80Ce-20Ti_SG were capable of effective light absorption as well as maintaining the oxygen vacancy sites, regardless of exposure to atmospheric conditions. The superior conversion rate exhibited by Ni/80Ce-20Ti_SG over that of Ni/50Ce-50Ti_SG further emphasized the importance of nickel deposit size on the photothermal activity of a ceria-titania-supported catalyst.

4. Conclusions

Ceria-titania-supported nickel catalysts were tested for their CO_2 reduction performance under light irradiation. When nickel was present on the supports, the catalysts were capable of greater absorption capacities within the Vis and NIR spectrum. The ceria-rich supports exhibited a greater degree of absorption in the Vis and NIR region (compared with the titania-rich supports), which was attributed to better nickel deposit dispersion invoked by the ceria presence. The increased absorption of this portion of the solar spectrum is anticipated to induce greater heating of the catalyst bed and, in turn, promote CO_2 methanation activity. In addition, CO_2 adsorption was facilitated by an increased presence of ceria, as it was promoted by surface defect generation within the ceria during the nickel pre-reduction stage. While titania was shown to be detrimental for nickel dispersion and CO_2 adsorption, it served an important function in stabilizing the oxygen vacancy-type defects within the support, thus better maintaining the CO_2 adsorption capacity during photothermal methanation. In addition to demonstrating the importance of a ceria presence for enhancing surface metal dispersion, this work shows that a titanium presence within the cubic ceria host lattice facilitates the stabilization of oxygen vacancy-type defects. Both of these characteristics are shown to be indispensable for high CO_2-to-methane conversion rates driven by light irradiation, as evidenced by the distinct dominance of Ni/50Ce-50Ti_SG and Ni/80Ce-20Ti_SG over the performance of the other catalysts and by the improvement in methanation rates upon a further increment in cerium concentration (i.e., from 50Ce∶50Ti to 80Ce∶20Ti). These findings demonstrate the importance of tailoring a composite metal oxide support so that the useful features of the individual components can be effectively harnessed and applied to photothermal catalytic reaction systems.

Acknowledgements

This work was financially supported by the Australian Research Council under the Laureate Fellowship Scheme (FL140100081). The authors would also like to acknowledge the facilities provided by the Solid State and Elemental Analysis Unit of the UNSW Mark Wainwright Analytical Center.

Compliance with ethics guidelines

Ee Teng Kho, Salina Jantarang, Zhaoke Zheng, Jason Scott, and Rose Amal declare that they have no conflict of interest or financial conflicts to disclose.

Supplementary Information

http://engineering.org.cn/EN/10.1016/J.ENG.2017.03.016
Figs. S1,S2

References

[1] Kale MJ, Avanesian T, Xin H, Yan J, Christopher P. Controlling catalytic selectivity on metal nanoparticles by direct photoexcitation of adsorbate-metal bonds. Nano Lett 2014;14(9):5405–12.
[2] Zhang X, Chen Y, Liu R, Tsai DP. Plasmonic photocatalysis. Rep Prog Phys 2013;76(4):046401.
[3] Lou Z, Wang Z, Huang B, Dai Y. Synthesis and activity of plasmonic photocatalysts. ChemCatChem 2014;6(9):2456–76.
[4] Cheng H, Fuku K, Kuwahara Y, Mori K, Yamashita H. Harnessing single-active plasmonic nanostructures for enhanced photocatalysis under visible light. J Mater Chem A 2015;3(10):5244–58.
[5] Jiang R, Li B, Fang C, Wang J. Metal/semiconductor hybrid nanostructures for plasmon—Enhanced applications. Adv Mater 2014;26(31):5274–309.

[6] Wang C, Ranasingha O, Natesakhawat S, Ohodnicki PR, Andio M, Lewis JP, et al. Visible light plasmonic heating of Au-ZnO for the catalytic reduction of CO_2. Nanoscale 2013;5(15):6968–74.
[7] Meng X, Wang T, Liu L, Ouyang S, Li P, Hu H, et al. Photothermal conversion of CO_2 into CH_4 with H_2 over Group VIII nanocatalysts: An alternative approach for solar fuel production. Angew Chem 2014;126(43):11662–6. German.
[8] Trovarelli A, Deleitenburg C, Dolcetti G, Lorca J. CO_2 methanation under transient and steady-state conditions over Rh/CeO_2 and CeO_2-promoted Rh/SiO_2: The role of surface and bulk ceria. J Catal 1995;151(1):111–24.
[9] Sakurai H, Haruta M. Carbon dioxide and carbon monoxide hydrogenation over gold supported on titanium, iron, and zinc oxides. Appl Catal A 1995;127(1–2):93–105.
[10] Wang W, Wang S, Ma X, Gong J. Recent advances in catalytic hydrogenation of carbon dioxide. Chem Soc Rev 2011;40(7):3703–27.
[11] Graciani J, Mudiyanselage K, Xu F, Baber AE, Evans J, Senanayake SD, et al. Highly active copper-ceria and copper-ceria-titania catalysts for methanol synthesis from CO_2. Science 2014;345(6196):546–50.
[12] Yang X, Kattel S, Senanayake SD, Boscoboinik JA, Nie X, Graciani J, et al. Low pressure CO_2 hydrogenation to methanol over gold nanoparticles activated on a CeO_x/TiO_2 interface. J Am Chem Soc 2015;137(32):10104–7.
[13] Park JB, Graciani J, Evans J, Stacchiola D, Ma S, Liu P, et al. High catalytic activity of $Au/CeO_x/TiO_2(110)$ controlled by the nature of the mixed-metal oxide at the nanometer level. Proc Natl Acad Sci USA 2009;106(13):4975–80.
[14] Park JB, Graciani J, Evans J, Stacchiola D, Senanayake SD, Barrio L, et al. Gold, copper, and platinum nanoparticles dispersed on $CeO_x/TiO_2(110)$ surfaces: High water-gas shift activity and the nature of the mixed-metal oxide at the nanometer level. J Am Chem Soc 2010;132(1):356–63.
[15] Graciani J, Plata JJ, Sanz JF, Liu P, Rodriguez JA. A theoretical insight into the catalytic effect of a mixed-metal oxide at the nanometer level: The case of the highly active $metal/CeO_x/TiO_2(110)$ catalysts. J Chem Phys 2010;132(10):104703.
[16] Farmer JA, Campbell CT. Ceria maintains smaller metal catalyst particles by strong metal-support bonding. Science 2010;329(5994):933–6.
[17] Cargnello M, Doan-Nguyen VV, Gordon TR, Diaz RE, Stach EA, Gorte RJ, et al. Control of metal nanocrystal size reveals metal-support interface role for ceria catalysts. Science 2013;341(6147):771–3.
[18] Kho ET, Lovell E, Wong RJ, Scott J, Amal R. Manipulating ceria-titania binary oxide features and their impact as nickel catalyst supports for low temperature steam reforming of methane. Appl Catal A 2017;530:111–24.
[19] Serpone N, Lawless D, Khairutdinov R. Size effects on the photophysical properties of colloidal anatase TiO_2 particles: Size quantization versus direct transitions in this indirect semiconductor? J Phys Chem 1995;99(45):16646–54.
[20] Chen HI, Chang HY. Synthesis of nanocrystalline cerium oxide particles by the precipitation method. Ceram Int 2005;31(6):795–802.
[21] Rahman MM, Im SH, Lee JJ. Enhanced photoresponse in dye-sensitized solar cells via localized surface plasmon resonance through highly stable nickel nanoparticles. Nanoscale 2016;8(11):5884–91.
[22] Bereketidou O, Goula M. Biogas reforming for syngas production over nickel supported on ceria-alumina catalysts. Catal Today 2012;195(1):93–100.
[23] Wootsch A, Descorme C, Duprez D. Preferential oxidation of carbon monoxide in the presence of hydrogen (PROX) over ceria-zirconia and alumina-supported Pt catalysts. J Catal 2004;225(2):259–66.
[24] Li Y, Wang X, Xie C, Song C. Influence of ceria and nickel addition to alumina-supported Rh catalyst for propane steam reforming at low temperatures. Appl Catal A 2009;357(2):213–22.
[25] De Rogatis L, Montini T, Casula MF, Fornasiero P. Design of $Rh@Ce_{0.2}Zr_{0.8}O_2$-Al_2O_3 nanocomposite for ethanol steam reforming. J Alloys Compd 2008;451(1–2):516–20.
[26] Cuauhtémoc I, Del Angel G, Torres G, Bertin V. Catalytic wet air oxidation of gasoline oxygenates using Rh/γ-Al_2O_3 and Rh/γ-Al_2O_3-CeO_2 catalysts. Catal Today 2008;(133–5):588–93.
[27] Amjad UES, Vita A, Galletti C, Pino L, Specchia S. Comparative study on steam and oxidative steam reforming of methane with noble metal catalysts. Ind Eng Chem Res 2013;52(44):15428–36.
[28] Vita A, Cristiano G, Italiano C, Pino L, Specchia S. Syngas production by methane oxy-steam reforming on Me/CeO_2 (Me = Rh, Pt, Ni) catalyst lined on cordierite monoliths. Appl Catal B 2015;162:551–63.
[29] Jain PK, Lee KS, El-Sayed IH, El-Sayed MA. Calculated absorption and scattering properties of gold nanoparticles of different size, shape, and composition: Applications in biological imaging and biomedicine. J Phys Chem B 2006;110(14):7238–48.
[30] Boudjahem AG, Monteverdi S, Mercy M, Bettahar MM. Nanonickel particles supported on silica. Morphology effects on their surface and hydrogenating properties. Catal Lett 2004;97(3):177–83.
[31] Boudjahem A, Monteverdi S, Mercy M, Bettahar MM. Study of nickel catalysts supported on silica of low surface area and prepared by reduction of nickel acetate in aqueous hydrazine. J Catal 2004;221(2):325–34.
[32] Cesteros Y, Salagre P, Medina F, Sueiras J. Synthesis and characterization of several $Ni/NiAl_2O_4$ catalysts active for the 1,2,4-trichlorobenzene hydrodechlorination. Appl Catal B 2000;25(4):213–27.
[33] Bal R, Tope BB, Das TK, Hegde SG, Sivasanker S. Alkali-loaded silica, a solid base: Investigation by FTIR spectroscopy of adsorbed CO_2 and its catalytic activity. J Catal 2001;204(2):358–63.
[34] Wang SG, Cao DB, Li YW, Wang J, Jiao H. Chemisorption of CO_2 on nickel surfaces. J Phys Chem B 2005;109(40):18956–63.
[35] Falconer JL, Zağli AE. Adsorption and methanation of carbon dioxide on a nickel/silica catalyst. J Catal 1980;62(2):280–5.
[36] Edmonds T, Pitkethly R. The adsorption of carbon monoxide and carbon dioxide at the (111) face of nickel observed by leed. Surf Sci 1969;15(1):137–63.
[37] Grosvenor AP, Biesinger MC, Smart RSC, McIntyre NS. New interpretations of XPS spectra of nickel metal and oxides. Surf Sci 2006;600(9):1771–9.
[38] Reddy BM, Khan A, Yamada Y, Kobayashi T, Loridant S, Volta JC. Structural characterization of CeO_2-TiO_2 and V_2O_5/CeO_2-TiO_2 catalysts by Raman and XPS techniques. J Phys Chem B 2003;107(22):5162–7.
[39] Sinha AK, Suzuki K. Preparation and characterization of novel mesoporous ceria-titania. J Phys Chem B 2005;109(5):1708–14.
[40] Rynkowski J, Farbotko J, Touroude R, Hilaire L. Redox behaviour of ceria-titania mixed oxides. Appl Catal A 2000;203(2):335–48.
[41] Habisreutinger SN, Schmidt-Mende L, Stolarczyk JK. Photocatalytic reduction of CO_2 on TiO_2 and other semiconductors. Angew Chem Int Ed 2013;52(29):7372–408.
[42] Navalón S, Dhakshinamoorthy A, Álvaro M, Garcia H. Photocatalytic CO_2 reduction using non-titanium metal oxides and sulfides. ChemSusChem 2013;6(4):562–77.
[43] Teramura K, Iguchi S, Mizuno Y, Shishido T, Tanaka T. Photocatalytic conversion of CO_2 in water over layered double hydroxides. Angew Chem 2012;124(32):8132–5. German.
[44] Lo CC, Hung CH, Yuan CS, Wu JF. Photoreduction of carbon dioxide with H_2 and H_2O over TiO_2 and ZrO_2 in a circulated photocatalytic reactor. Sol Energy Mater Sol Cells 2007;91(19):1765–74.
[45] Tada S, Shimizu T, Kameyama H, Haneda T, Kikuchi R. Ni/CeO_2 catalysts with high CO_2 methanation activity and high CH_4 selectivity at low temperatures. Int J Hydrogen Energ 2012;37(7):5527–31.